



1 **Four dimensional quantification of Kelvin-Helmholtz**  
2 **instabilities in the polar summer mesosphere using**  
3 **volumetric radar imaging**

4 **J. L. Chau<sup>1</sup>, J. M. Urco<sup>1</sup>, V. Avsarkisov<sup>1</sup>, J. P. Vierinen<sup>2</sup>, R. Latteck<sup>1</sup>, C. M.**  
5 **Hall<sup>3</sup>, and M. Tsutsumi<sup>4</sup>**

6 <sup>1</sup>Leibniz Institute of Atmospheric Physics, University of Rostock, Kühlungsborn, Germany.

7 <sup>2</sup>Department of Physics and Technology, UiT - The Arctic University of Norway, Tromsø, Norway

8 <sup>3</sup>Tromsø Geophysical Observatory, UiT - The Arctic University of Norway, Tromsø, Norway

9 <sup>4</sup>National Institute of Polar Research, Tokyo, Japan

10 **Key Points:**

- 11 • Four-dimensional quantification of a clearly resolved Kelvin-Helmholtz Instabil-  
12 ity event observed with volumetric radar imaging.
- 13 • The Richardson number is estimated to be much less than 0.25, using indepen-  
14 dent measurements.
- 15 • The Froude number is estimated to be close to 1 (weak stratification) and a high  
16 buoyancy Reynolds number  $\sim 2.5 \times 10^4$  is estimated.

---

Corresponding author: Jorge L. Chau, [chau@iap-kborn.de](mailto:chau@iap-kborn.de)

This article has been accepted for publication and undergone full peer review but has not been through the copyediting, typesetting, pagination and proofreading process which may lead to differences between this version and the Version of Record. Please cite this article as doi: 10.1029/2019GL086081

**Abstract**

We present and characterize in time and three spatial dimensions a Kelvin-Helmholtz Instability (KHI) event from polar mesospheric summer echoes (PMSE) observed with the Middle Atmosphere Alomar Radar System. We use a newly developed radar imaging mode, which observed PMSE intensity and line of sight velocity with high temporal and angular resolution. The identified KHI event occurs in a narrow layer of 2.4 km thickness centered at 85 km altitude, is elongated along North-South direction, presents separation between billows of  $\sim 8$  km in the East-West direction, and its billow width is  $\sim 3$  km. The accompanying vertical gradients of the horizontal wind are between 35 and 45 m/s/km and vertical velocities inside the billows are  $\pm 12$  m/s. Based on the estimated Richardson ( $< 0.25$ ), horizontal Froude ( $\sim 0.8$ ), and buoyancy Reynolds ( $\sim 2.5 \times 10^4$ ) numbers, the observed event is a KHI that occurs under weak stratification and generates strong turbulence.

**1 Introduction**

In the mesosphere lower thermosphere (MLT) region, atmospheric instabilities account for wave dissipation, turbulence generation, and turbulent mixing. One of the most prominent MLT instabilities is the Kelvin-Helmholtz Instability (KHI) that occurs preferentially on strong shear of the horizontal wind due to gravity waves, tides, planetary waves and mean flows. A necessary condition for KHI to occur is that the Richardson number ( $Ri$ ) is less than 0.25 (e.g., Miles, 1961). These instabilities play an important role in the transport and deposition of energy and momentum (e.g., Thorpe, 1973; Fritts & Rastogi, 1985; Hecht, 2004; Hecht et al., 2007).

KHIs in the MLT have been inferred from a number of ground-based instruments (e.g., Lehmacher et al., 2007; Hysell et al., 2012) or characterized by using information from complementary instrumentation (e.g., Hecht, 2004; Li, Liu, Swenson, Hecht, & Robinson, 2005). For example, ripples observed in airglow imagers have been associated with KHIs and characterized with the aid of other supporting ground based observations, e.g., winds from specular meteor radars (SMRs), medium frequency radars or lidars. In most cases, one or two dimensions of the events are not available. For example, in the case of airglow imagers, the vertical dimension is not. To overcome the relative large thickness of the airglow layer of a few kilometers, high resolution ground- and balloon-based images of noctilucent clouds (NLCs) have been recently shown to be useful to study KHI

49 with high spatial and temporal resolution (e.g., Baumgarten & Fritts, 2014; Fritts et al.,  
50 2014, 2019).

51 The relatively limited number of observations of KHIs in the mesosphere show a  
52 wide variety of spatial structures and alignments with respect to the background wind.  
53 These observations are being complemented with direct numerical simulations (DNS)  
54 and large eddy simulations (LES). The studies are particularly suitable for MLT cases,  
55 since they are characterized by high Reynolds numbers, i.e.,  $\mathcal{O}(10^3)$  (e.g. Fritts et al.,  
56 2014; Marino et al., 2015). For example, the comparison of KHIs from NLC observations  
57 with numerical simulations indicate a turbulent viscosity much larger (5 to 40 times) than  
58 the true kinematic viscosity at the NLC altitude (e.g., Fritts et al., 2014).

59 In this work we quantify in four dimensions a KHI event observed in the polar meso-  
60 sphere during summer. This unique observation has been made with the Middle Atmo-  
61 sphere Alomar Radar System (MAARSY) located in northern Norway. The clear quan-  
62 tification is possible due to an improved radar imaging of Polar Mesospheric Summer  
63 echoes (PMSEs) that utilizes a Multiple-Input Multiple-output (MIMO) approach de-  
64 veloped by Urco et al. (2018). Currently there is general consensus that PMSE are gen-  
65 erated by atmospheric turbulence, but require the presence of free electrons and charged  
66 iced particles (e.g., Varney et al., 2011, and references therein) to increase the signal to  
67 noise ratio of the echoes sufficiently to make them observable with relatively low power  
68 atmospheric radars. Given that PMSE intensity depends on different parameters (tur-  
69 bulence, electron density, ice-particle density, electron density gradients, etc.), for this  
70 work we only rely in PMSE as tracer of the undergoing atmospheric dynamics.

71 The present paper is organized as follows. We first start with a brief description  
72 of the high resolution four dimensional radar observations and examples of what can be  
73 measured. Then we present the wind dynamics around the event under study, includ-  
74 ing a description of how the background winds are obtained. The specific dynamics dur-  
75 ing the event and the KHI observations from PMSE are shown in Section 4. We end up  
76 with the quantification of the KHI event and the discussion of its parameters and atmo-  
77 spheric conditions.

## 2 High resolution four dimensional radar observations

Mesosphere Stratosphere Troposphere (MST) radars are able to measure the neutral wind from Bragg scale ( $\lambda/2$ ) atmospheric irregularities, where  $\lambda$  is the radar wavelength (e.g., Woodman & Guillén, 1974). Traditionally they have provided atmospheric measurements with relative high temporal and vertical resolution over a particular region (e.g., Fukao et al., 2011; Luce et al., 2012; Lehmacher et al., 2007). Using phased arrays with electronic beam steering, modern atmospheric radars also provide horizontal information using a multi-beam approach (e.g., Fukao et al., 1985; Latteck et al., 2012; Sato et al., 2014). Although the horizontal coverage is extended with this approach, the relatively long correlation time of atmospheric targets, the effects of a truncated antenna aperture, and the way electronic phasing is done (i.e., from pulse to pulse), the achieved angular and temporal resolutions have not been good enough to resolve atmospheric structures in the scales of kilometer- and minute-resolution, at least in the mesosphere (e.g., Stober et al., 2018).

Besides the multi-beam approach, in-beam radar imaging of ionospheric and atmospheric irregularities has been implemented. In the case of ionospheric irregularities, most of the implementations have been successful at separating spatial and temporal features (e.g., Hysell & Chau, 2006; Hysell et al., 2014). In the case of radar imaging of atmospheric irregularities, previous efforts have obtained results with varying degrees of success. In most cases, the procedures implemented (hardware and signal processing) were not good enough to resolve spatial scales smaller than the beam width (e.g. Chau & Woodman, 2001; Yu et al., 2001). Sommer and Chau (2016) using MAARSY with a wide beam transmitting beam and the Capon imaging technique, were able to identify PMSE structures smaller than the beam width on a statistical basis.

Recently, Urco et al. (2019) introduced a new radar imaging technique that makes use of a MIMO approach and a Maximum Entropy regularization technique. The MIMO approach has been implemented using time diversity, i.e., three different 1/6ths of MAARSY's full array were interleaved in time. On reception fifteen smaller sections called Hexagons were used. This combination resulted in an effective 50% larger receiving aperture diameter than previous experiments, and forty-five effective receiving channels. The achieved angular resolution is close to  $0.6^\circ$  (i.e., 0.9 km at 85 km), at least 6 times better than

109 using the multibeam approach at MAARSY. More specific details of this implementa-  
110 tion and other PMSE imaging examples can be found in Urco et al. (2019).

111 In Figure 1 we show an example of a volumetric PMSE radar image using six dif-  
112 ferent two-dimensional cuts. There are four horizontal cuts at 83.8, 84.6, 85.4, and 86.2  
113 km altitudes in the first row. The second row contains two vertical cuts, an East-West  
114 cut at  $x = 0$  km, and a North-South cut at  $y = 0$  km. These cuts were obtained on  
115 July 17, 2017 at 00:55:43 UT with 40 seconds of integration. The  $(x, y)$  coordinates are  
116 with respect to the center of the MAARSY array. Doppler line-of-sight velocity infor-  
117 mation is shown with color. Red represents velocities away from the radar (around -10  
118 m/s) and blue velocities towards (around 10 m/s) the radar. Green represents veloci-  
119 ties close to zero. The maximum velocities displayed are  $\pm 15$  m/s. The intensity of the  
120 colors represents signal-to-noise ratio (SNR) on logarithmic scale, following the conven-  
121 tion used in Urco et al. (2019).

122 Given that the obtained resolution is  $\sim 1$  km in the horizontal direction at PMSE  
123 altitudes, most of the shown features are of atmospheric origin. In the case of the cen-  
124 tral altitudes, the PMSE strengths are at least two orders of magnitude stronger than  
125 at the edges, allowing the observation of atmospheric dynamics associated to weaker echoes  
126 and smaller scale dynamics.

127 From Figure 1, we can see ripples in all four horizontal cuts, elongated in the  $y$  di-  
128 rection. The dimensions of the billows associated to the ripples are 2.4 and 3.0 km in  
129 the  $z$  and  $x$  directions, respectively. Below we describe in more detail the spatial and tem-  
130 poral characteristics around of this event and discuss its origin in terms of a KHI.

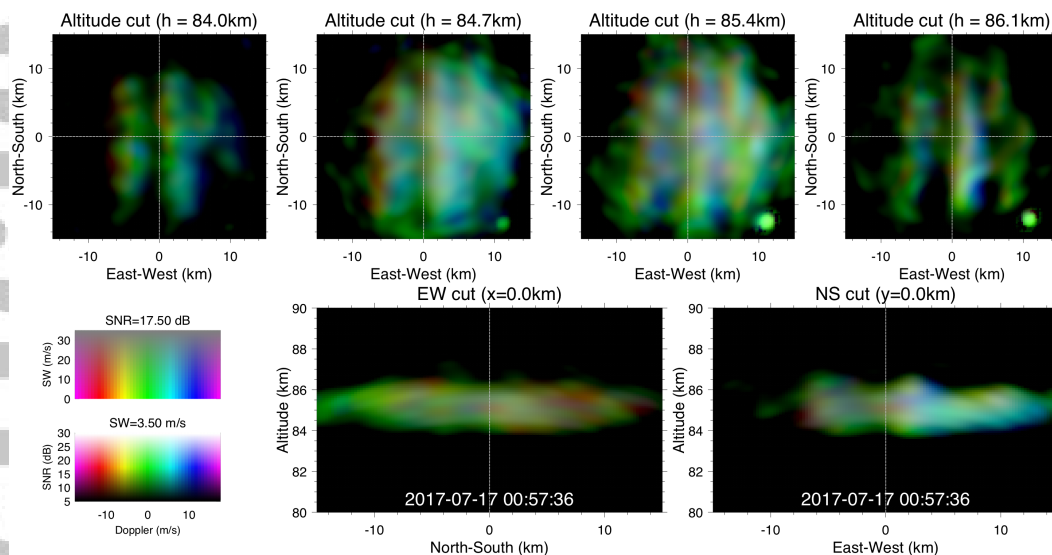


**Figure 1.** Two dimensional cuts of a PMSE example obtained on July 17, 2017 at 00:54:43 UT: horizontal cuts at 83.8, 84.6, 85.4, and 86.2 km altitudes in the first row, respectively; and vertical East-West and North-South cuts at  $x = 0$  and  $y = 0$ , respectively, in the second row. Doppler and signal-to-noise ratio (SNR) are color coded. SW in the legend stands for spectral width.

131 The temporal evolution of all these six two-dimensional cuts around the KHI event  
 132 under study can be found in Movie S1 that is included in the supplementary material.  
 133 Note that these types of observations have been obtained during a larger special cam-  
 134 paign in July 2017. A summary range-time-Doppler intensity plot of the 32 hours of mea-  
 135 surements obtained during this campaign can be found in Urco et al. (2019), Figure 2.

### 136 3 Background wind dynamics

137 The occurrence of KHI is related to the background dynamics. Specifically  $Ri$  less  
 138 than 0.25 is a necessary condition for KHI to occur, where  $Ri$  is a function of the hor-  
 139 izontal wind, i.e.,  $Ri = N^2 / (dU/dz)^2$ . Here  $N$  is the Brunt-Väisälä frequency, and  $dU/dz$   
 140 is the vertical gradient of the horizontal wind ( $U$ ).

141 Although PMSEs are good tracers of the wind dynamics (e.g., Rapp et al., 2008),  
 142 measurements can only be obtained where there are PMSEs, and they are not present  
 143 at all altitudes and times. To overcome this, we have obtained the mean mesospheric winds  
 144 by using measurements from two closely-located SMRs, specifically Tromsø (19.22°E,

145 69.58°N) and Andenes (16.04°E, 69.27°N). The combination of both systems allows us  
146 to have a higher meteor count and to obtain a zero-order Taylor expansion of the wind  
147 field (mean winds) with temporal and vertical sampling of 5 min and 500 m, using win-  
148 dows of 1 hour and 2 km, respectively (Chau et al., 2017). In order to observe the mean  
149 wind in a relatively localized region around the imaged radar volume, we have used only  
150 meteors that occur within 120 km horizontal radius around MAARSY.

151 Figure 2 shows the obtained background wind dynamics around the time of the KHI  
152 event of interest in this work. Specifically, we show the magnitude and direction of the  
153 horizontal wind ( $U$ ), and the magnitude and direction of the vertical gradient of the hor-  
154 izontal wind ( $dU/dz$ ), in the first and second column respectively. Eastward and north-  
155 ward directions are represented by 0 and 90 degrees, respectively. PMSEs were observed  
156 between the horizontal black lines in all four figures. The black rectangles indicate the  
157 time and altitude of the KHI event below.

158 From a cursory look, the region within the rectangle is characterized by: a strong  
159 westward wind at the bottom and weak wind tending northward at the top. During this  
160 time,  $|U|$  is the smallest above this region. As expected, the associated  $|dU/dz|$  is strong  
161 at the bottom of the rectangle. Note that there are other regions of strong  $|dU/dz|$ , many  
162 of them not occurring at PMSE altitudes.



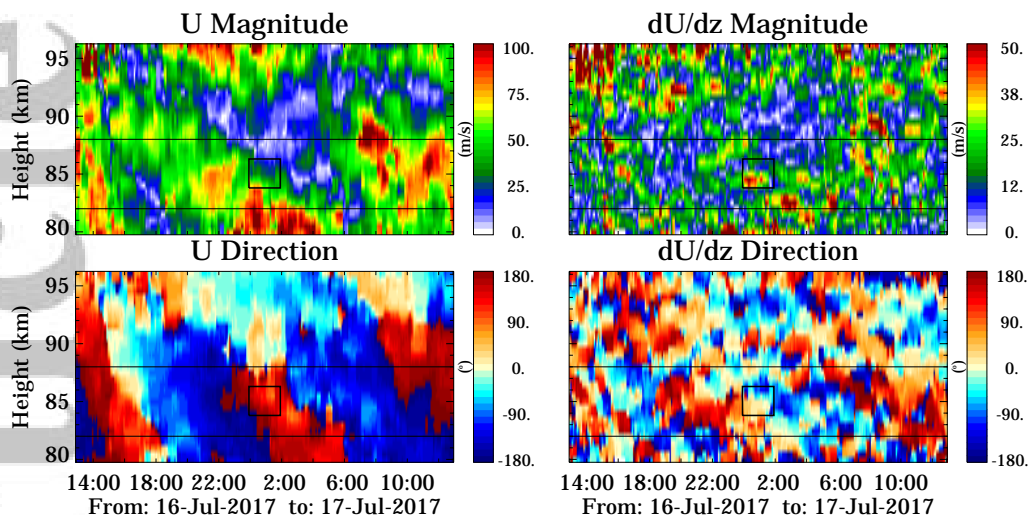


**Figure 2.** Mesospheric dynamics obtained with Tromsø and Andenes SMRs: (first column) Horizontal wind ( $U$ ) magnitude and direction; (second column) Magnitude and direction of the vertical gradient of the horizontal wind ( $dU/dz$ ). PMSE altitudes are in between horizontal lines. The rectangle indicates the time and altitude of a KHI event.

## 4 Results

In this section we focus on the altitude dynamics around July 17, 2017 at 0055 UT event using SMR winds, as well as on the temporal and spatial evolution using high resolution PMSE images, i.e., around the KHI event of interest.

### 4.1 Altitude profiles of dynamics

In Figure 2 we showed the general dynamics around (a few hours) the event in question. To quantify better those dynamics, in Figure 3, we show the altitude profiles of the variables shown in Figure 2 in addition to the zonal ( $u$ ) and meridional ( $v$ ) components. The profiles are color coded in time, around  $\pm 60$  minutes from the KHI event. The values at the time of the KHI event are shown with diamonds. In this plot, the horizontal lines indicate the altitude region of the KHI event.

The salient dynamical features at the central time of the event are: (a) before the event  $u$  was stronger and  $v$  weaker at the bottom than after the event, (b) the effective  $|dU/dz|$  was stronger before than after the event at the bottom, 45 m/s/km compared to 35 m/s/km, (c) at the event the strong wind at the bottom was westward, while at



178 the top was to the North-West, (d) the direction of  $dU/dz$  changes significantly from bot-  
 179 tom to top. Therefore, the obtained  $|dU/dz|$  values are strong and might produced KHI.  
 180 Below we use these values to discuss the occurrence of a KHI event and its quantifica-  
 181 tion.

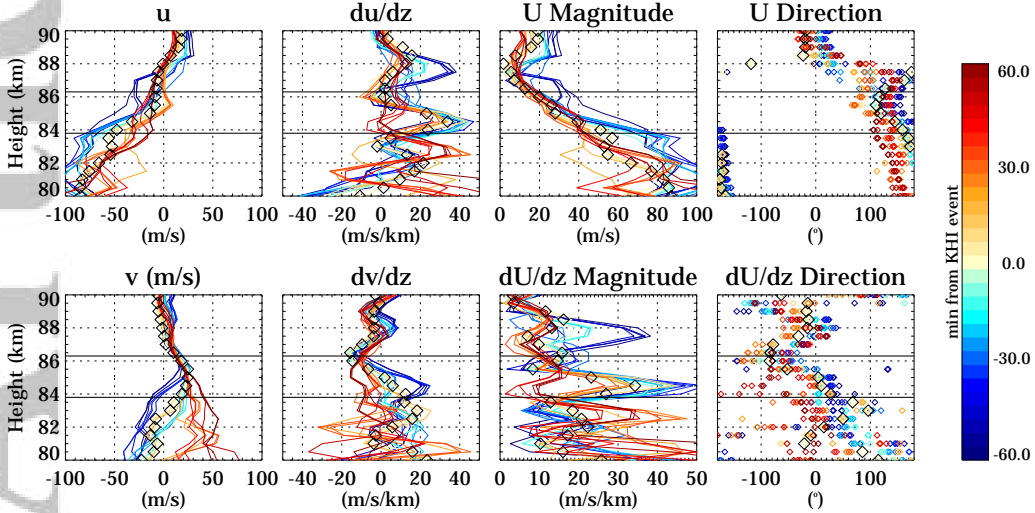


**Figure 3.** Altitude profiles of dynamics around the July 17, 2019 at 0055 UT over Andenes:  $u$ ,  $du/dz$ ,  $v$ ,  $dv/dz$ ,  $|U|$ ,  $U$  direction,  $|dU/dz|$  and  $dU/dz$  direction, color coded in time (around  $\pm 60$  minutes). Diamonds indicate the profile closer to the KHI event. Horizontal lines denote the bottom and top of the event.

## 182 4.2 Temporal evolution of 2D cuts

183 Figure 4 shows the temporal evolution of horizontal cuts at  $y = 0$ , and  $x = 0$ ,  
 184 respectively. These cuts are shown for the same altitudes as the horizontal cuts presented  
 185 in Figure 1, i.e., 83.8, 84.6, 85.4, and 86.2 km, respectively. Doppler and SNR informa-  
 186 tion are color coded with hue and intensity. This presentation is similar to those used  
 187 in airglow imagers (so-called Keograms), but resolved in a narrow altitude layer and with  
 188 Doppler information included. The dotted lines represent the time and space cuts shown  
 189 in Figure 1.

190 In all four altitude cuts there are organized ripples mainly drifting westward at  $\sim 30$   
 191 m/s (i.e., 9 km in 5 minutes). Although we are combining Doppler and SNR informa-  
 192 tion into one image They are elongated in the North-South direction with a length of  
 193 at least 20 km (see second column). The width of each of the ripples is less than 3 km

194 ( $L_x$ ) along the propagation direction, and the separation between them  $\sim 8$  km ( $\lambda_x$ ). In  
 195 the transverse direction (i.e., NS),  $\sim 2$ -km structures ( $L_y$ ) are observed, but not as clearly  
 196 as the structures in the EW direction. At the altitude edges (i.e., 83.8 and 86.2 km), the  
 197 ripples are more clearly observed than at the center altitudes where they coexist with  
 198 PMSEs showing less organized structures. In the relative small observing area, up to six  
 199 ripples are observed at the center altitudes.

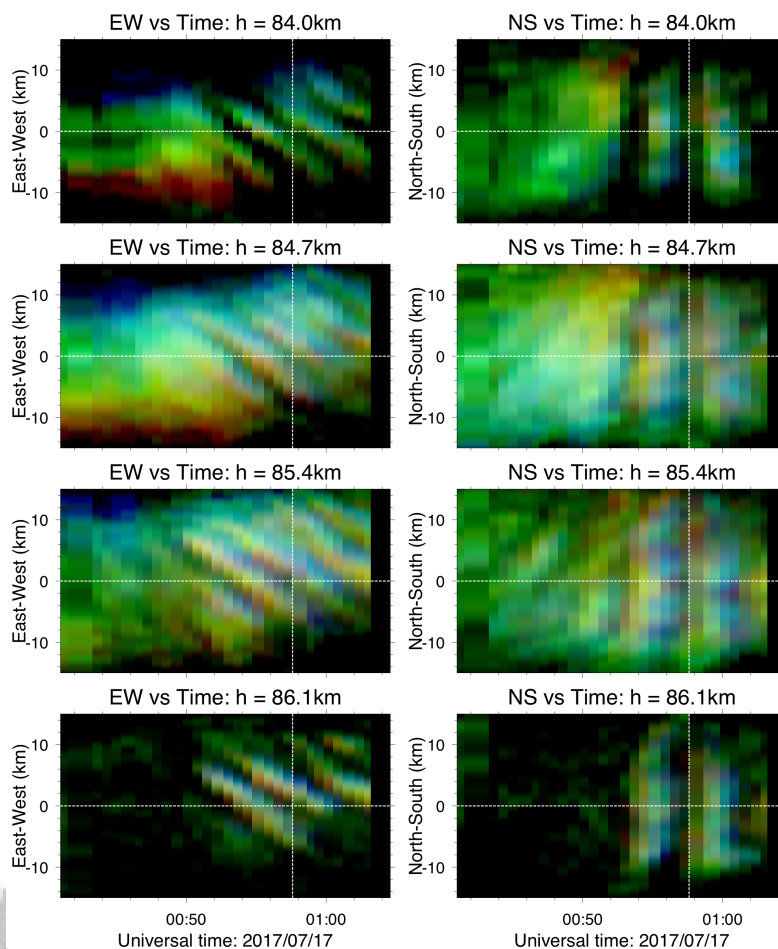


**Figure 4.** Temporal evolution of EW (left) and NS (right) cuts at  $y = 0$  and  $x = 0$ , respectively. Doppler and SNR are color coded as before.

## 200 5 Discussion

201 Taking into account the PMSE imaging information and the background dynam-  
 202 ics, we can clearly see that the observed ripples are associated with a KHI event. Us-  
 203 ing an expected average buoyancy period of 400 s (e.g. Rapp et al., 2004) and the mea-

204 measured  $S = |dU/dz|$  values (40 m/s/km) (see Figure 3), the resulting  $Ri$  is  $\sim 0.15$ , i.e.,  
 205 less than 0.25 that is necessary for sustained turbulence and thus occurrence of KHIs.  
 206 However,  $Ri < 0.25$  is not a sufficient condition for KHI occurrence. For example, ac-  
 207 cording to Kunze et al. (1990) the KHI growth rate is proportional to  $S - 2N$  over a  
 208 large range of  $Ri$ , then small  $N$  would result on small  $Ri$  and also small growth rates.  
 209 Our event is associated with a relative large growth rate and is expected to be accom-  
 210 panied by a large growth rate (e.g., Hysell et al., 2012). However the estimation of growth  
 211 rate required precised measurements of wind and temperature profiles (or  $N^2$ ), that we  
 212 do not have. Therefore, we shall discuss other characteristics that support our conclu-  
 213 sion, i.e., that the event is indeed a KHI.

214 In Figure 5 we show two dimensional cuts ( $xz$  and  $xy$ ) at one particular time to  
 215 quantify the KHI event better. Given that vertical resolution of the measured images  
 216 ( $I_m$ ) is only 450 m, and that there is the coexistence of other structures, in panels 5b  
 217 and 5e we show the fluctuations corresponding to panels 5a and 5d. Such a fluctuating  
 218 component ( $I_{\text{wave}}^c$ ) has been obtained for each Doppler image  $c$  (i.e., red, green, and blue,  
 219 see above) independently, by estimating a low-pass filtered version ( $I_{\text{mean}}^c$ ) as follows:

$$I_{\text{wave}}^c = \frac{I_m^c - I_{\text{mean}}^c}{I_{\text{mean}}^c} \quad (1)$$

220 The low-pass filtered images have been obtained using a two-dimensional running mean  
 221 smoothing with (20, 20) and (20,1) points for the  $xy$  and  $xz$  cuts, respectively. A sim-  
 222 ilar procedure is used in airglow wave analysis (e.g., Garcia et al., 1997). The maximum  
 223 values plotted for each of the Doppler images are  $\pm 25\%$ .

224 The fluctuating components clearly show that the billows present upward veloc-  
 225 ities to the West and downward velocities to the East, in all three billows shown. The  
 226 billow occurring at  $x = -5$  km, is wider than the other two billows and show “cat’s-  
 227 eye” structure (Figure 5b). In the NS direction, there are 2-km scale structures along  
 228 the billows, i.e., in the transverse direction to the propagation (Figure 5e). Perhaps these  
 229 transverse structures are related to secondary billows reported in DNS simulations (e.g.,  
 230 Fritts et al., 2014), but our resolution is not high enough to resolve them better.

231 In panels 5c and 5f we show simplified versions of the observed images and to help  
 232 with the interpretation we overplot the measured wind velocities, either from PMSE (ver-  
 233 tical winds) or from the multistatic SMR (horizontal winds). Based on these results and  
 234 sketches, the observed features of our KHI event are:  $L_x = 3$  km,  $L_z = 2.4$  km (thick-

235 ness in  $z$ ),  $\lambda_x = 8$  km,  $U_z = 12$  m/s (i.e., the billow root-mean square vertical veloc-  
 236 ity, half the maximum minus minimum vertical velocity), and propagation speed in the  
 237 westward direction of 30 m/s. The propagation velocity is very similar to the mean back-  
 238 ground wind at the KHI altitudes, i.e., implying a small phase velocity.

239 Additional evidence that supports the KHI interpretation of this event are the thick-  
 240 ness to separation ratio of  $L_z/\lambda_x \sim 0.3$  and the high vertical velocities accompanying  
 241 the billows ( $\pm 12$  m/s). If we compare this ratio to numerical studies with high Reynolds  
 242 numbers, the expected  $Ri$  is between 0.10 and 0.15 (e.g., Thorpe, 1973).

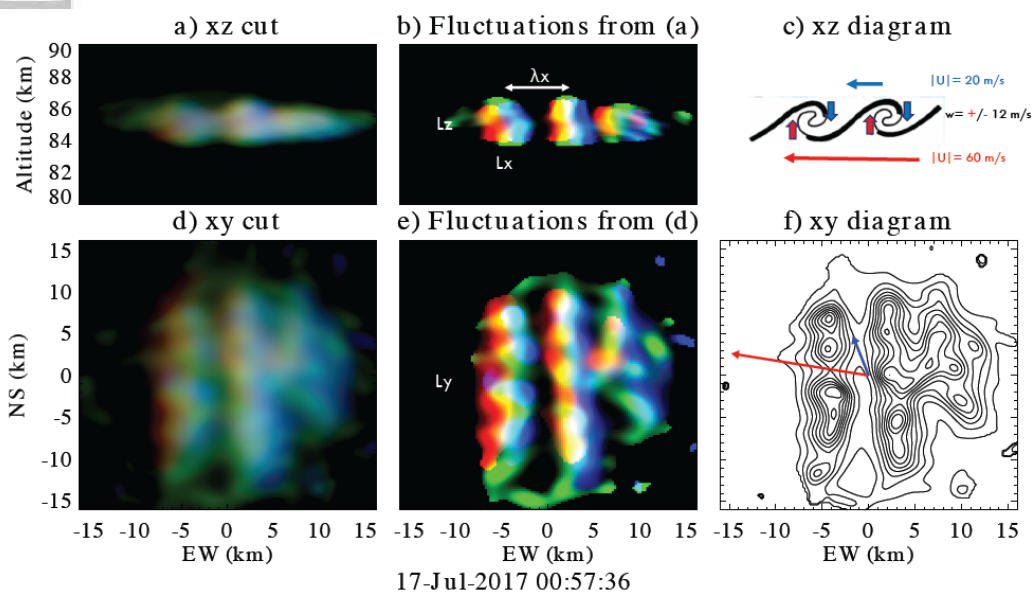


**Figure 5.** 2D cuts of PMSEs Images at 00:57:36 on July 17, 2017 for: (a) xz, and (d) xy, similar to Figure 1. Their fluctuating components obtained using Eq. 1 are shown in panels (b) and (e), respectively. Sketches for the two cuts are shown in panels (c) and (f), respectively. The horizontal velocities at the bottom and top of the layers are indicated with red and blue thin arrows, respectively.

243 Using these length-scales and vertical velocity, it is possible to apply the theory of  
 244 stratified turbulence to explore some more details about the observed KHI event. By mak-  
 245 ing the assumption that  $L_x$ ,  $L_z$ , and  $U_z$  are the characteristic lengths and velocity scales  
 246 of this event, and using the continuity equation, which has a non-divergent form in strat-

247 ified turbulence (Davidson, 2013), we can obtain the following constraint:

$$\frac{L_x}{U_x} \sim \frac{L_z}{U_z}. \quad (2)$$

248 From (2) it is possible to derive the characteristic horizontal RMS velocity:  $U_x \sim U_z L_x / L_z =$   
 249 15 m/s.

250 A turbulent dissipation rate ( $\epsilon$ ) can be obtained from the definition of an integral  
 251 length-scale  $L_{int} \sim U^3 / \epsilon$ , which is an outer scale in homogeneous and isotropic turbu-  
 252 lence. In the present case, the turbulent dissipation rate is defined as:

$$\epsilon = C_\epsilon \frac{U_x^3}{L_x} = 1.125 \text{ W/kg}, \quad (3)$$

253 here we assume that the constant  $C_\epsilon = 1.0$  (e.g., Gargett, 1999, Figure 8). At this point,  
 254 however, it should be noted that the turbulent dissipation rate obtained through Eq. 3  
 255 is a local value of  $\epsilon$  for the observed KHI event. This value is comparable to the largest  
 256 values measured with rockets near the polar summer mesopause (e.g., Lübken et al., 2002,  
 257 Figure 2).

258 There is an another scaling definition of  $L_z$ , namely  $L_z = U_x / N$  (e.g., Billant &  
 259 Chomaz, 2001). It indicates that the vertical scale of the turbulence is a thickness of the  
 260 stratification level and it is defined exclusively by the dynamics of the stratified turbu-  
 261 lent flow. With the usage of the new definition of  $L_z$  it is possible to obtain the local buoy-  
 262 ancy frequency value, which is  $N = U_x / L_z = 0.00625 \text{ s}^{-1}$ . This corresponds to a buoy-  
 263 ancy period of  $\sim 1005\text{s}$ , which is more than twice the value used above that represents  
 264 average background conditions. This is not surprising since  $N$  is known to be highly vari-  
 265 able in the mesosphere (e.g., Li, Liu, & Swenson, 2005). The new estimate of  $N$  is ob-  
 266 tained locally and suggest that stratification effects inside the KHI event are negligibly  
 267 small.

268 The theory of strongly stratified turbulence states that there are only two non-dimensional  
 269 parameters that exclusively define the turbulence regime in sheared and stratified flows  
 270 (Lindborg, 2006; Brethouwer et al., 2007). These two parameters are the horizontal Froude  
 271 number  $Fr$  and the buoyancy Reynolds number  $Re_b$  defined as:

$$Fr = \frac{\epsilon}{NU_x^2} = \frac{U_x}{L_x N} \quad (4)$$

$$Re_b = \frac{\epsilon}{\nu N^2} = \frac{U_x^3}{\nu N^2 L_x} \quad (5)$$

$$(6)$$

272 where  $\nu$  is the kinematic viscosity. In the present study, it is possible to calculate these  
273 two parameters for the KHI event with values of  $U_x$ ,  $N$  and  $L_x$  estimated above. Thus,  
274 we get  $Fr = 0.8$  and  $Re_b = 2.5 \times 10^4$ . We have assumed  $\nu = 1.15 \text{ m}^2/\text{s}$ , which is ex-  
275 pected in the polar summer mesosphere. The high horizontal Froude number  $Fr > \mathcal{O}(10^{-2})$   
276 indicates a weak stratification and that the observed turbulence event is generated through  
277 the KHI instability, while large  $Re_b$  suggests a wide inertial subrange of the kinetic and  
278 potential energy spectra of the present event.

279 The scaling analysis applied in the present study supports the observational result  
280 obtained with volumetric radar imaging without invoking a highly uncertain Miles-Howard  
281 criterion for turbulence existence, i.e.,  $Ri < 0.25$  (e.g., Galperin et al., 2007). The lo-  
282 cal values of  $\epsilon$  and  $N$  confirm the presence of very strong turbulence inside the detected  
283 structures, while the negligible degree of anisotropy indicates an absence of the strat-  
284 ification effects inside these structures.

## 285 6 Concluding Remarks

286 We have presented a high resolution volumetric radar imaging measurement of KHI  
287 in the polar summer mesopause. The observation provides PMSE intensity and line of  
288 sight velocity measured as a function of time and three spatial dimensions. To our knowl-  
289 edge, this is the first spatially resolved measurement of mesospheric KHI observed with  
290 radar in four dimensions.

291 The event is composed of up to six elongated ripples in the NS direction, propa-  
292 gating to the West at  $\sim 30 \text{ m/s}$  with separation between billows of  $\sim 8 \text{ km}$ , a layer thick-  
293 ness of  $2.4 \text{ km}$ , and billow width of less than  $3 \text{ km}$ . The necessary conditions for being  
294 a KHI are satisfied, i.e.,  $Ri < 0.25$  using expected buoyancy periods, measured  $|dU/dz|$ ,  
295 scaling analysis, and comparisons with previous numerical simulations. Furthermore, based  
296 on the observed parameters, the event occurs with  $Fr \sim 1$  and high  $Re_b$ , indicating con-  
297 ditions of weak stratification and a clear turbulent nature of the observed event, i.e., KHI.

298 Although we have focused on just one KHI event, we are certain that many more  
299 events and not only KHI can be characterized with the type of PMSE volumetric imag-  
300 ing shown in this work. Given that not all the time one can separate easily the contri-  
301 butions of gravity waves and turbulence, one could quantify statistically such contribu-

302 tions by exploiting the multidimensional data with second order statistics of the radial  
303 velocities, as it has been proposed by Vierinen et al. (2019).

304 The new volumetric radar imaging capability can augment existing lidar, radar,  
305 and airglow measurements used for studies of small-scale dynamics. As indicated by Fritts  
306 et al. (2014), these types of small-scale multi-dimensional observations coupled with mod-  
307 eling capabilities will enable a more complete quantification of small-scale dynamics, and  
308 a better parameterization in large-scale general circulation atmospheric models.

### 309 Acknowledgments

310 This work was supported by the Deutsche Forschungsgemeinschaft (DFG, German Re-  
311 search Foundation) under SPP 1788 (CoSIP)-CH1482/3-1. The authors thank useful com-  
312 ments from David Fritts and Raffaele Marino that help us interpret our observations.

313 The wind data (“mmaria\_par\*.h5”) and PMSE imaging data (under “Event01” direc-  
314 tory) can be found both in HDF5 format at <ftp://ftp.iap-kborn.de/data-in-publications/ChauGRL2019>.

315 In the case of the PMSE Imaging data, each brightness file corresponds to  $\sim 40$  seconds  
316 integration and contains  $129 \times 129 \times 101 \times 16$  points, representing x, y, z, and frequency bins.

317 The corresponding meta data is contained in “metadata.h5”.

### 318 References

319 Baumgarten, G., & Fritts, D. C. (2014). Quantifying kelvin-helmholtz instability  
320 dynamics observed in noctilucent clouds: 1. methods and observations. *Journal of Geophysical Research: Atmospheres*, *119*(15), 9324–9337. Retrieved from  
321 <http://dx.doi.org/10.1002/2014JD021832> (2014JD021832) doi: 10.1002/  
322 2014JD021832

324 Billant, P., & Chomaz, J.-M. (2001). Self-similarity of strongly stratified inviscid  
325 flows. *Physics of Fluids*, *13*(6), 1645–1651. doi: 10.1063/1.1369125

326 Brethouwer, G., Billant, P., Lindborg, E., & Chomaz, J.-M. (2007). Scaling analysis  
327 and simulation of strongly stratified turbulent flows. *Journal of Fluid Mechan-*  
328 *ics*, *585*, 343368. doi: 10.1017/S0022112007006854

329 Chau, J. L., Stober, G., Hall, C. M., Tsutsumi, M., Laskar, F. I., & Hoffmann, P.  
330 (2017). Polar mesospheric horizontal divergence and relative vorticity measure-  
331 ments using multiple specular meteor radars. *Radio Science*, *52*(7), 811–828.  
332 Retrieved from <http://dx.doi.org/10.1002/2016RS006225> (2016RS006225)



333 doi: 10.1002/2016RS006225

334 Chau, J. L., & Woodman, R. F. (2001). Three-dimensional coherent radar imag-  
335 ing at jicamarca: comparison of different inversion techniques. *Journal of*  
336 *Atmospheric and Solar-Terrestrial Physics*, 63(2), 253 - 261. Retrieved from  
337 <http://www.sciencedirect.com/science/article/pii/S1364682600001425>  
338 (Radar applications for atmosphere and ionosphere research - PIERS 1999)  
339 doi: [https://doi.org/10.1016/S1364-6826\(00\)00142-5](https://doi.org/10.1016/S1364-6826(00)00142-5)

340 Davidson, P. A. (2013). *Turbulence in Rotating, Stratified and Electrically Conduct-*  
341 *ing Fluids*. Cambridge University Press.

342 Fritts, D. C., Baumgarten, G., Wan, K., Werne, J., & Lund, T. (2014). Quantify-  
343 ing kelvin-helmholtz instability dynamics observed in noctilucent clouds: 2.  
344 modeling and interpretation of observations. *Journal of Geophysical Research:*  
345 *Atmospheres*, 119(15), 9359–9375. Retrieved from [http://dx.doi.org/](http://dx.doi.org/10.1002/2014JD021833)  
346 [10.1002/2014JD021833](http://dx.doi.org/10.1002/2014JD021833) (2014JD021833) doi: 10.1002/2014JD021833

347 Fritts, D. C., Miller, A. D., Kjellstrand, C. B., Geach, C., Williams, B. P., Kaifler,  
348 B., ... Randall, C. E. (2019). Pmc turbo: Studying gravity wave and in-  
349 stability dynamics in the summer mesosphere using polar mesospheric cloud  
350 imaging and profiling from a stratospheric balloon. *Journal of Geophysi-*  
351 *cal Research: Atmospheres*, 124(12), 6423-6443. Retrieved from [https://](https://agupubs.onlinelibrary.wiley.com/doi/abs/10.1029/2019JD030298)  
352 [agupubs.onlinelibrary.wiley.com/doi/abs/10.1029/2019JD030298](https://agupubs.onlinelibrary.wiley.com/doi/abs/10.1029/2019JD030298) doi:  
353 [10.1029/2019JD030298](https://doi.org/10.1029/2019JD030298)

354 Fritts, D. C., & Rastogi, P. K. (1985). Convective and dynamical instabilities due  
355 to gravity wave motions in the lower and middle atmosphere: Theory and  
356 observations. *Radio Science*, 20(6), 1247-1277. Retrieved from [https://](https://agupubs.onlinelibrary.wiley.com/doi/abs/10.1029/RS020i006p01247)  
357 [agupubs.onlinelibrary.wiley.com/doi/abs/10.1029/RS020i006p01247](https://agupubs.onlinelibrary.wiley.com/doi/abs/10.1029/RS020i006p01247)  
358 doi: 10.1029/RS020i006p01247

359 Fukao, S., Luce, H., Mega, T., & Yamamoto, M. K. (2011). Extensive stud-  
360 ies of large-amplitude kelvinhelmholtz billows in the lower atmosphere  
361 with vhf middle and upper atmosphere radar. *Quarterly Journal of*  
362 *the Royal Meteorological Society*, 137(657), 1019-1041. Retrieved from  
363 <https://rmets.onlinelibrary.wiley.com/doi/abs/10.1002/qj.807> doi:  
364 [10.1002/qj.807](https://doi.org/10.1002/qj.807)

365 Fukao, S., Sato, T., Tsuda, T., Kato, S., Wakasugi, K., & Makihira, T. (1985, Nov).

- 366 The mu radar with an active phased array system, 1. antenna and power am-  
367 plifiers. *Radio Science*, 20(6), 1155-1168. doi: 10.1029/RS020i006p01155
- 368 Galperin, B., Sukoriansky, S., & Anderson, P. S. (2007). On the critical Richard-  
369 son number in stably stratified turbulence. *Atmos. Sci. Lett.*, 8, 65-69. doi: 10  
370 .1002/asl.153
- 371 Garcia, F. J., Taylor, M. J., & Kelley, M. C. (1997, Oct). Two-dimensional spectral  
372 analysis of mesospheric airglow image data. *Appl. Opt.*, 36(29), 7374-7385.  
373 Retrieved from <http://ao.osa.org/abstract.cfm?URI=ao-36-29-7374> doi:  
374 10.1364/AO.36.007374
- 375 Gargett, A. E. (1999). Velcro measurement of turbulence kinetic energy dissipation  
376 rate  $\epsilon$ . *Journal of Atmospheric and Oceanic Technology*, 16(12), 1973-1993.  
377 doi: 10.1175/1520-0426(1999)016(1973:VMOTKE)2.0.CO;2
- 378 Hecht, J. H. (2004). Instability layers and airglow imaging. *Reviews of Geo-*  
379 *physics*, 42(1). Retrieved from [https://agupubs.onlinelibrary.wiley.com/](https://agupubs.onlinelibrary.wiley.com/doi/abs/10.1029/2003RG000131)  
380 [doi/abs/10.1029/2003RG000131](https://agupubs.onlinelibrary.wiley.com/doi/abs/10.1029/2003RG000131) doi: 10.1029/2003RG000131
- 381 Hecht, J. H., Liu, A. Z., Walterscheid, R. L., Franke, S. J., Rudy, R. J., Taylor,  
382 M. J., & Pautet, P.-D. (2007). Characteristics of short-period wavelike features  
383 near 87 km altitude from airglow and lidar observations over maui. *Journal*  
384 *of Geophysical Research: Atmospheres*, 112(D16). Retrieved from [https://](https://agupubs.onlinelibrary.wiley.com/doi/abs/10.1029/2006JD008148)  
385 [agupubs.onlinelibrary.wiley.com/doi/abs/10.1029/2006JD008148](https://agupubs.onlinelibrary.wiley.com/doi/abs/10.1029/2006JD008148) doi:  
386 10.1029/2006JD008148
- 387 Hysell, D. L., Aveiro, H. C., & Chau, J. L. (2014). Ionospheric irregularities. In  
388 *Modeling the ionospherethermosphere system* (p. 217-240). American Geophys-  
389 ical Union (AGU). Retrieved from [https://agupubs.onlinelibrary.wiley](https://agupubs.onlinelibrary.wiley.com/doi/abs/10.1002/9781118704417.ch18)  
390 [.com/doi/abs/10.1002/9781118704417.ch18](https://agupubs.onlinelibrary.wiley.com/doi/abs/10.1002/9781118704417.ch18) doi: 10.1002/9781118704417  
391 .ch18
- 392 Hysell, D. L., & Chau, J. L. (2006). Optimal aperture synthesis radar imaging. *Ra-*  
393 *dio Sci.*, 41, doi:10.1029/2005RS003383.
- 394 Hysell, D. L., Nossa, E., Larsen, M. F., Munro, J., Smith, S., Sulzer, M. P., & Gon-  
395 zalez, S. A. (2012). Dynamic instability in the lower thermosphere inferred from  
396 irregular sporadic e layers. *Journal of Geophysical Research: Space Physics*,  
397 117(A8). Retrieved from [https://agupubs.onlinelibrary.wiley.com/doi/](https://agupubs.onlinelibrary.wiley.com/doi/abs/10.1029/2012JA017910)  
398 [abs/10.1029/2012JA017910](https://agupubs.onlinelibrary.wiley.com/doi/abs/10.1029/2012JA017910) doi: 10.1029/2012JA017910

- 399 Kunze, E., Williams III, A. J., & Briscoe, M. G. (1990). Observations of shear  
400 and vertical stability from a neutrally buoyant float. *Journal of Geophys-*  
401 *ical Research: Oceans*, 95(C10), 18127-18142. Retrieved from [https://](https://agupubs.onlinelibrary.wiley.com/doi/abs/10.1029/JC095iC10p18127)  
402 [agupubs.onlinelibrary.wiley.com/doi/abs/10.1029/JC095iC10p18127](https://agupubs.onlinelibrary.wiley.com/doi/abs/10.1029/JC095iC10p18127)  
403 doi: 10.1029/JC095iC10p18127
- 404 Latteck, R., Singer, W., Rapp, M., Vandeppeer, B., Renkowitz, T., Zecha, M., &  
405 Stober, G. (2012, Jan). MAARSY: The new MST radar on Andøya –  
406 System description and first results. *Radio Sci.*, 47(1), RS1006. doi:  
407 10.1029/2011RS004775
- 408 Lehmacher, G., Guo, L., Kudeki, E., Reyes, P., Akgiray, A., & Chau, J. (2007).  
409 High-resolution observations of mesospheric layers with the jicamarca vhf  
410 radar. *Advances in Space Research*, 40(6), 734 - 743. Retrieved from  
411 <http://www.sciencedirect.com/science/article/pii/S0273117707005406>  
412 doi: <https://doi.org/10.1016/j.asr.2007.05.059>
- 413 Li, F., Liu, A. Z., & Swenson, G. R. (2005). Characteristics of instabilities in the  
414 mesopause region over maui, hawaii. *Journal of Geophysical Research: Atmo-*  
415 *spheres*, 110(D9). Retrieved from [https://agupubs.onlinelibrary.wiley](https://agupubs.onlinelibrary.wiley.com/doi/abs/10.1029/2004JD005097)  
416 [.com/doi/abs/10.1029/2004JD005097](https://agupubs.onlinelibrary.wiley.com/doi/abs/10.1029/2004JD005097) doi: 10.1029/2004JD005097
- 417 Li, F., Liu, A. Z., Swenson, G. R., Hecht, J. H., & Robinson, W. A. (2005). Ob-  
418 servations of gravity wave breakdown into ripples associated with dynami-  
419 cal instabilities. *Journal of Geophysical Research: Atmospheres*, 110(D9).  
420 Retrieved from [https://agupubs.onlinelibrary.wiley.com/doi/abs/](https://agupubs.onlinelibrary.wiley.com/doi/abs/10.1029/2004JD004849)  
421 [10.1029/2004JD004849](https://agupubs.onlinelibrary.wiley.com/doi/abs/10.1029/2004JD004849) doi: 10.1029/2004JD004849
- 422 Lindborg, E. (2006). The energy cascade in a strongly stratified fluid. *Journal of*  
423 *Fluid Mechanics*, 550, 207242. doi: 10.1017/S0022112005008128
- 424 Lübken, F.-J., Rapp, M., & Hoffmann, P. (2002). Neutral air turbulence and tem-  
425 peratures in the vicinity of polar mesosphere summer echoes. *Journal of Geo-*  
426 *physical Research: Atmospheres*, 107(D15), ACL 9-1-ACL 9-10. Retrieved  
427 from [https://agupubs.onlinelibrary.wiley.com/doi/abs/10.1029/](https://agupubs.onlinelibrary.wiley.com/doi/abs/10.1029/2001JD000915)  
428 [2001JD000915](https://agupubs.onlinelibrary.wiley.com/doi/abs/10.1029/2001JD000915) doi: 10.1029/2001JD000915
- 429 Luce, H., Nishi, N., Caccia, J.-L., Fukao, S., Yamamoto, M. K., Mega, T., ...  
430 Nakazato, M. (2012). Kelvin-helmholtz billows generated at a cirrus cloud  
431 base within a tropopause fold/upper-level frontal system. *Geophysical Research*

- 432 *Letters*, 39(4). Retrieved from [https://agupubs.onlinelibrary.wiley.com/](https://agupubs.onlinelibrary.wiley.com/doi/abs/10.1029/2011GL050120)  
433 [doi/abs/10.1029/2011GL050120](https://agupubs.onlinelibrary.wiley.com/doi/abs/10.1029/2011GL050120) doi: 10.1029/2011GL050120
- 434 Marino, R., Rosenberg, D., Herbert, C., & Pouquet, A. (2015, November). In-  
435 terplay of waves and eddies in rotating stratified turbulence and the link  
436 with kinetic-potential energy partition. *Europhysics Letters*, 112(4). doi:  
437 10.1209/0295-5075/112/49001
- 438 Miles, J. W. (1961). On the stability of heterogeneous shear flows. *Journal of Fluid*  
439 *Mechanics*, 10(4), 496508. doi: 10.1017/S0022112061000305
- 440 Rapp, M., Strelnikov, B., Mllemann, A., Lbken, F.-J., & Fritts, D. C. (2004). Tur-  
441 bulence measurements and implications for gravity wave dissipation during  
442 the macwave/midas rocket program. *Geophysical Research Letters*, 31(24).  
443 Retrieved from [https://agupubs.onlinelibrary.wiley.com/doi/abs/](https://agupubs.onlinelibrary.wiley.com/doi/abs/10.1029/2003GL019325)  
444 [10.1029/2003GL019325](https://agupubs.onlinelibrary.wiley.com/doi/abs/10.1029/2003GL019325) doi: 10.1029/2003GL019325
- 445 Rapp, M., Strelnikova, I., Latteck, R., Hoffmann, P., Hoppe, U.-P., Haggstrom, I.,  
446 & Rietveld, M. (2008). Polar mesosphere summer echoes (PMSE) studied at  
447 Bragg wavelengths of 2.8 m, 67 cm, and 16 cm. *Journal of Atmospheric and*  
448 *Solar Terrestrial Physics*, 70, 947–961. doi: 10.1016/j.jastp.2007.11.005
- 449 Sato, K., Tsutsumi, M., Sato, T., Nakamura, T., Saito, A., Tomikawa, Y., . . . Ya-  
450 manouchi, T. (2014). Program of the antarctic syowa mst/is radar (pansy).  
451 *Journal of Atmospheric and Solar-Terrestrial Physics*, 118, 2 - 15. Re-  
452 trieved from [http://www.sciencedirect.com/science/article/pii/](http://www.sciencedirect.com/science/article/pii/S1364682613002447)  
453 [S1364682613002447](http://www.sciencedirect.com/science/article/pii/S1364682613002447) (Recent progress from networked studies based around  
454 MST radar) doi: <https://doi.org/10.1016/j.jastp.2013.08.022>
- 455 Sommer, S., & Chau, J. L. (2016). Patches of polar mesospheric summer echoes  
456 characterized from radar imaging observations with maarsy. *Annales Geophys-*  
457 *icae*, 34(12), 1231–1241. Retrieved from [https://www.ann-geophys.net/34/](https://www.ann-geophys.net/34/1231/2016/)  
458 [1231/2016/](https://www.ann-geophys.net/34/1231/2016/) doi: 10.5194/angeo-34-1231-2016
- 459 Stober, G., Sommer, S., Schult, C., Latteck, R., & Chau, J. L. (2018). Observation  
460 of kelvin–helmholtz instabilities and gravity waves in the summer mesopause  
461 above andenes in northern norway. *Atmospheric Chemistry and Physics*,  
462 18(9), 6721–6732. Retrieved from [https://www.atmos-chem-phys.net/18/](https://www.atmos-chem-phys.net/18/6721/2018/)  
463 [6721/2018/](https://www.atmos-chem-phys.net/18/6721/2018/) doi: 10.5194/acp-18-6721-2018
- 464 Thorpe, S. A. (1973). Experiments on instability and turbulence in a strati-

- 465 fied shear flow. *Journal of Fluid Mechanics*, 61(4), 731751. doi: 10.1017/  
466 S0022112073000911
- 467 Urco, J. M., Chau, J. L., Milla, M. A., Vierinen, J. P., & Weber, T. (2018). Co-  
468 herent mimo to improve aperture synthesis radar imaging of field-aligned  
469 irregularities: First results at jicamarca. *IEEE Transactions on Geoscience and*  
470 *Remote Sensing*, PP(99), 1-11. doi: 10.1109/TGRS.2017.2788425
- 471 Urco, J. M., Chau, J. L., Weber, T., & Latteck, R. (2019). Enhancing the spatio-  
472 temporal features of polar mesosphere summer echoes using coherent mimo  
473 and radar imaging at maarsy. *Atmospheric Measurement Techniques*, 12,  
474 955–969. doi: 10.5194/amt-12-955-2019
- 475 Varney, R. H., Kelley, M. C., Nicolls, M. J., Heinselman, C. J., & Collins, R. L.  
476 (2011, September). The electron density dependence of polar meso-  
477 spheric summer echoes. *J. Atmos. Sol. Terr. Phys.*, 73, 2153-2165. doi:  
478 10.1016/j.jastp.2010.07.020
- 479 Vierinen, J., Chau, J. L., Charuvil, H., Urco, J. M., Clahsen, M., Avsarkisov, V.,  
480 ... Volz, R. (2019). Observing mesospheric turbulence with specular meteor  
481 radars: A novel method for estimating second-order statistics of wind veloc-  
482 ity. *Earth and Space Science*, 6(7), 1171-1195. Retrieved from [https://](https://agupubs.onlinelibrary.wiley.com/doi/abs/10.1029/2019EA000570)  
483 [agupubs.onlinelibrary.wiley.com/doi/abs/10.1029/2019EA000570](https://agupubs.onlinelibrary.wiley.com/doi/abs/10.1029/2019EA000570) doi:  
484 10.1029/2019EA000570
- 485 Woodman, R. F., & Guillén, A. (1974). Radar observations of winds and turbulence  
486 in the stratosphere and mesosphere. *J. Atmos. Sci.*, 31(2), 493-505.
- 487 Yu, T.-Y., Palmer, R. D., & Chilson, P. B. (2001). An investigation of scat-  
488 tering mechanisms and dynamics in pmse using coherent radar imaging.  
489 *Journal of Atmospheric and Solar-Terrestrial Physics*, 63(17), 1797 - 1810.  
490 Retrieved from [http://www.sciencedirect.com/science/article/pii/](http://www.sciencedirect.com/science/article/pii/S136468260100058X)  
491 [S136468260100058X](http://www.sciencedirect.com/science/article/pii/S136468260100058X) doi: [https://doi.org/10.1016/S1364-6826\(01\)00058-X](https://doi.org/10.1016/S1364-6826(01)00058-X)